Relative Enhanced Diffusivity in Prostate Cancer: Protocol Optimization and Diagnostic Potential

Daniel C. Billdal, MSRP,[1*] Peter T. While, PhD,[2] Kirsten M. Selnæs, PhD,[2] Mohammed R. S. Sunoqrot, MS,[1] Sverre Langørgen, MD, PhD,[1,2] Helena Bertilsson, MD, PhD,[3,4] Tone F. Bathen, PhD,[1,5] and Mattijs Elschot, PhD[1,2]

Background: Relative enhanced diffusivity (RED) is a potential biomarker for indirectly measuring perfusion in tissue using diffusion-weighted magnetic resonance imaging (MRI) with 3 *b* values.
Purpose: To optimize the RED MRI protocol for the prostate, and to investigate its potential for prostate cancer (PCa) diagnosis.
Study Type: Prospective.
Population: Ten asymptomatic healthy volunteers and 35 patients with clinical suspicion of PCa.
Sequence: 3T T_2- and diffusion-weighted MRI with *b* values: b = 0, 50, [100], 150, [200], 250, [300], 400, 800 s/mm^2 (values in brackets were only used for patients).
Assessment: Monte Carlo simulations were performed to assess noise sensitivity of RED as a function of intermediate *b* value. Volunteers were scanned 3 times to assess repeatability of RED. Patient data were used to investigate RED's potential for discriminating between biopsy-confirmed cancer and healthy tissue, and between true and false positive radiological findings.
Statistical Tests: Within-subject coefficient of variation (WCV) to assess repeatability and receiver-operating characteristic curve analysis and logistic regression to assess diagnostic performance of RED.
Results: The repeatability was acceptable (WCV = 0.2-0.3) for all intermediate *b* values tested, apart from b = 50 s/mm^2 (WCV = 0.3-0.4). The simulated RED values agreed well with the experimental data, showing that an intermediate *b* value between 150-250 s/mm^2 minimizes noise sensitivity in both peripheral zone (PZ) and transition zone (TZ). RED calculated with the *b* values 0, 150 and 800 s/mm^2 was significantly higher in tumors than in healthy tissue in both PZ ($P < 0.001$, area under the curve [AUC] = 0.85) and PZ + TZ ($P < 0.001$, AUC = 0.84). RED was shown to aid apparent diffusion coefficient (ADC) in differentiating between false-positive findings and true-positive PCa in the PZ (AUC; RED = 0.71, ADC = 0.74, RED+ADC = 0.77).
Data Conclusion: RED is a repeatable biomarker that may have value for prostate cancer diagnosis. An intermediate *b* value in the range of 150-250 s/mm^2 minimizes the influence of noise and maximizes repeatability.
Level of Evidence: 2
Technical Efficacy Stage: 1

J. MAGN. RESON. IMAGING 2019.

View this article online at wileyonlinelibrary.com. DOI: 10.1002/jmri.27011

Received Sep 20, 2019, Accepted for publication Nov 19, 2019.

*Address reprint requests to: D.C.B., NTNU, MR Centre, Olav Kyrres gate 9, MTFS, 3rd floor, south, 7030 Trondheim, Norway. E-mail: danielcb@stud.ntnu.no
Contract grant sponsor: Faculty of Medicine and Health Sciences, NTNU, Norwegian University of Science and Technology, financed the Medical Student Research Program (to D.C.B.); The researcher position of ME is financed by the Contract grant sponsor: Central Norway Regional Health Authority; Contract grant number: 17/38297 (to M.E.).

From the [1]Department of Circulation and Medical Imaging, NTNU, Norwegian University of Science and Technology, Trondheim, Norway; [2]Department of Radiology and Nuclear Medicine, St. Olavs Hospital, Trondheim University Hospital, Trondheim, Norway; [3]Department of Cancer Research and Molecular Medicine, NTNU, Norwegian University of Science and Technology, Trondheim, Norway; [4]Department of Urology, St. Olavs Hospital, Trondheim University Hospital, Trondheim, Norway; and [5]St. Olavs Hospital, Trondheim University Hospital, Trondheim, Norway

Additional supporting information may be found in the online version of this article

MULTIPARAMETRIC MAGNETIC RESONANCE IMAGING (mpMRI) of the prostate is traditionally performed with the combination of anatomical T_2-weighted (T_2W) imaging and functional diffusion-weighted and dynamic contrast-enhanced (DCE) imaging. mpMRI plays an important role in the diagnosis and management of prostate cancer (PCa), especially after the Prostate Imaging Reporting and Data System (PI-RADS) guidelines were introduced.[1]

Diffusion-weighted imaging (DWI) probes the diffusion of water molecules within different tissues, without the need for an extraneous contrast agent.[2] Especially, apparent diffusion coefficient (ADC) maps have proven to be useful for PCa diagnosis.[3] However, the mathematical model underlying the calculation of ADC assumes monoexponential signal decay as a function of b value due to pure diffusion of water molecules. In reality, most tumors also have a perfusion component resulting from microcirculation of blood in the capillary network, which contributes to signal decay at lower b values.[4]

More advanced diffusion models, such as the intravoxel incoherent motion (IVIM) model, take this perfusion component into account. IVIM was introduced by Le Bihan et al[5] in 1988 and describes the signal decay as biexponential in tissues with a strong perfusion component. The IVIM model remains popular in the DWI community because of the apparent direct association with physical properties of the tissue microvasculature,[6] and improvements in comparison to the ADC model for prostate tumor detection[7] and grading[8] have been reported. IVIM is correlated with DCE-derived parameters in renal tumors,[9] head and neck tumors,[10] and breast tumors,[11] and has therefore been proposed as an alternative to DCE imaging to probe tissue microvasculature without the use of contrast agents.[12] IVIM, however, typically requires ≥10 different b values to probe the signal decay, and thus comes at the cost of a substantial increase in acquisition time, which limits its use in routine clinical practice.

Teruel et al recently introduced a novel marker for microcirculation, called relative enhanced diffusivity (RED),[13] which only requires the acquisition of one low, one intermediate, and one high b value. RED expresses the relative change in ADC between lower and higher b value regimes and is expected to be higher in more perfused tissue. Teruel et al[13] found that RED could distinguish malignant from benign breast cancer lesions with high sensitivity and specificity. Furthermore, the study found a moderate correlation between RED and breast cancer microcirculation parameters from DCE MRI. The latter finding is especially interesting for PCa, as biparametric MRI, leaving out the DCE sequence, shows promise in the clinic.[14–17] The reduced use of gadolinium contrast is also desirable because of the cost and the risk of gadolinium accumulation, with unknown long-term effects.[18]

While et al[19] showed with Monte Carlo simulations that the choice of the intermediate b value is important for the calculation of RED when it comes to minimizing sensitivity to noise, and that an optimal intermediate b value for breast and liver tissue was ~100 s/mm^2 and 50 s/mm^2, respectively. While et al[19] also demonstrated that RED can be regarded as a reparameterization of the simplified IVIM estimates for the perfusion fraction f and the diffusion coefficient D, also obtained with only three b values, as first proposed by Le Bihan et al.[5]

The purpose of this study was to optimize the RED MRI protocol for the prostate, by finding the optimal intermediate b value that minimizes the impact of noise, and to investigate the diagnostic potential of RED as a biomarker for PCa in comparison to ADC, as well as D and f from simplified IVIM.

Materials and Methods

Patients and Asymptomatic Healthy Volunteers

This study concerns prospectively acquired MRI data, approved by the Regional Committee for Medical and Health Research Ethics (REC Mid Norway, identifiers 2017/576 and 2014/1289). Ten asymptomatic healthy volunteers and 35 patients were prospectively recruited between 2017 to 2018. All participants provided written informed consent.

This study included two cohorts. The volunteer cohort consisted of 10 asymptomatic healthy volunteers (median age: 31; range: 24–43 years), each scanned at three different timepoints. The median interval between scans 1 and 2, and 2 and 3, was 12 and 15 days, respectively. This cohort was used to investigate the repeatability of region of interest (ROI)-based RED.

The patient cohort consisted of 35 patients referred for a prebiopsy MRI exam due to clinical suspicion of PCa (median age: 65; range: 51–80 years). Patients were subdivided into an optimization cohort with PI-RADS-negative patients (n = 18), and a diagnostic cohort with PI-RADS-positive (PI-RADS ≥3 as defined by PI-RADS v2,[3] scored by a radiologist) patients (n = 17). The optimization cohort was used for protocol optimization and comparison to simulated RED values in healthy tissue. The patients in the diagnostic cohort all underwent systematic biopsies or targeted MRI / transrectal ultrasound (TRUS) fusion biopsy, the results of which were considered the gold standard for the presence of cancer. The diagnostic cohort was therefore used to investigate the diagnostic potential of RED. Patient characteristics for all the cohorts and lesion information for the diagnostic cohort are shown in Table 1.

Imaging Protocol

All imaging was performed with a 3T Magnetom Skyra scanner (Siemens Healthineers, Erlangen, Germany). The imaging protocol for both cohorts included T_2W and DWI as described below.

The T_2W imaging for the volunteer cohort was performed with a turbo spin-echo (TSE) sequence with repetition time / echo time (TR/TE) = 7740/104 msec; 384 × 384 matrix size; 0.5 × 0.5 mm in-plane resolution; 3.0 mm slice thickness; and 26 transverse slices. The DWI acquisition was performed in the right–left

TABLE 1. Patient Characteristics for the Volunteer, Optimization, and Diagnostic Cohort, and Lesion Information for the Diagnostic Cohort

Patient table		
Patient characteristics		
Volunteer cohort		
Volunteers	N = 10	
Mean age (range)	31.1 years (24–43)	
Mean days between scan 1 and 2	11.9 days	
Mean days between scan 2 and 3	18.8 days	
Optimization cohort		
Patients	N = 18	
Mean age (range)	64.6 years (52–77)	
Mean PSA (SD)	6.9 ng/mL (3.14)	
Mean prostate volume (SD)	51.3 ml (24.6)	
Diagnostic cohort		
Patients	N = 17	
Mean age (range)	66.5 years (51–80)	
Mean PSA (SD)	11.9 ng/mL (14.3)	
Mean prostate volume (SD)	46.9 ml (23.1)	
Lesion information		
Diagnostic cohort	Peripheral zone	Transition zone
Lesions by zone	n = 14	n = 6
False positive lesions by zone	n = 10	n = 2
Mean TP lesion size (SD)	19.8 mm (13.5)	19.0 mm (9.1)
Mean FP lesion size (SD)	13.2 mm (6.9)	15.0 mm (8.5)
PIRADS 3 (TP lesions)	n = 7 (3)	n = 3 (2)
PIRADS 4 (TP lesions)	n = 8 (3)	n = 1 (1)
PIRADS 5 (TP lesions)	n = 9 (8)	n = 4 (3)
Gleason score 3 + 3	n = 1	n = 2
Gleason score 3 + 4	n = 9	n = 1
Gleason score 4 + 3	n = 0	n = 3
Gleason score 4 + 4	n = 1	n = 0
Gleason score 4 + 5	n = 3	n = 0

SD (standard deviation), PSA (prostate specific antigen), PZ (peripheral zone), TZ (transition zone), TP (true positive), FP (false positive).

phase-encoding direction, using a spin-echo sequence with single-shot echo planar imaging (SS-EPI) readout. Six b value scans (0, 50, 150, 250, 400, 800 s/mm^2) were acquired in three orthogonal diffusion directions using the following settings: TR/TE = 4400/63 msec; 128 × 120 matrix size; 2.0 × 2.0 mm in-plane resolution; 3.0 mm slice thickness; 6 averages (8 averages for b = 800); and 26 transverse slices. Trace images were used for further processing.

The T_2W imaging for the patient cohort was performed with a TSE sequence with TR/TE = 5330/104; 384 × 384 matrix size; 0.5 × 0.5 mm in-plane resolution; 3.0 mm slice thickness; and 26 transverse slices. The DWI acquisition was performed in the right–left phase-encoding direction, using a spin-echo sequence with SS-EPI readout. Nine b value scans (0, 50, 100, 150, 200, 250, 300, 400, 800 s/mm^2) were acquired in three orthogonal diffusion directions using the following settings: TR/TE = 3400/63 msec; 128 × 120 matrix size; 2.0 × 2.0 mm in-plane resolution; 3.0 mm slice thickness; 3 averages (8 averages for b = 800); and 20 transverse slices. Trace images were used for further processing.

Region of Interest Delineation

In the volunteer cohort, T_2W images were used as a reference to place four circular regions-of-interest (ROIs) (diameter 8 mm) in both the peripheral zone (PZ) and transition zone (TZ) in the diffusion-weighted images on the day 1 scans. The same eight ROIs were manually replicated for the scans on days 2 and 3.

In the optimization cohort, T_2W images were used as a reference to place six circular ROIs (diameter 8 mm) in healthy-appearing tissue in both the PZ and TZ in the diffusion-weighted images. In the diagnostic cohort, one circular ROI (diameter 8 mm) was placed in each PI-RADS-positive PZ or TZ lesion in the ADC images. ROIs of the same size were placed in contralateral healthy-appearing tissue in the PZ and TZ. An example of ROI placement and size for a false-positive case in the diagnostic cohort is shown in Appendix 1. ROIs in the volunteer and optimization cohort were of the same size.

Data Analysis

RED values were calculated for all voxels of the selected ROIs in the volunteer cohort. RED, ADC, and the simplified IVIM parameters (D_s and f_s) were calculated for all voxels of the selected ROIs in the diagnostic and optimization cohort. Full IVIM parameters (D, f, and D^*) were estimated for all voxels of the selected ROIs in the

optimization cohort (for the purpose of generating synthetic data). ADC values were calculated by fitting the monoexponential signal decay function to the b values 0, 150, and 800 s/mm^2, given by Eq. 1, where S_b is the signal for a given b value and S_0 is the signal for b = 0 s/mm^2:

$$\frac{S_b}{S_0} = e^{-b \times ADC} \quad (1)$$

RED values were calculated as given by Eq. 2,[13] where ADC_{low} was calculated between b = 0 s/mm^2 and the intermediate b value (ie, b = 50, 150, 250, or 400 s/mm^2 for the volunteers, or b = 50, 100, 150, 200, 250, 300, or 400 s/mm^2 for the patients), and ADC_{high} between the intermediate b value and b = 800 s/mm^2:

$$\mathrm{RED}\,(\%) = 100 \times \left(\frac{\mathrm{ADC_{low}}}{\mathrm{ADC_{high}}} - 1\right) \quad (2)$$

The parameters from the full IVIM[5] model were estimated by fitting a biexponential function given by Eq. 3, using a segmented approach with automatic thresholding,[20] which includes a diffusion coefficient (D), a pseudodiffusion (cf. perfusion) coefficient (D*), and a perfusion fraction parameter (f):

$$S_b/S_0 = (1-f)e^{-bD} + fe^{-b(D+D^*)} \quad (3)$$

For simplified IVIM using three b values, D* was explicitly omitted and $D_S \sim D$ and $f_S \sim f$ were calculated as given by Eqs. 4 and 5, respectively, where b_{interm} is the intermediate b value:

$$D_S = ADC_{high} \quad (4)$$

$$f_S = 1 - e^{-b_{interm}(ADC_{low} - ADC_{high})} \quad (5)$$

Simulations

Monte Carlo calculations were performed to simulate the sensitivity of RED to noise as a function of intermediate b value, as previously described by While et al.[19] The full IVIM parameter estimates from the nine b value data of the optimization cohort were used exclusively to generate synthetic data for this purpose. The mean and standard deviation for these estimates were used to define normal distributions, from which 10,000 samples were then drawn randomly for each full IVIM parameter (D, D*, f).

For every set (10,000) of the three synthetic full IVIM parameters, normalized signal (S_b/S_0) was simulated using Eq. 3 and subsequently corrupted by three different levels of Rician noise, to produce datasets with SNRs (signal-to-noise ratios) of 10, 20, and 40 with respect to the normalized signal at b = 0 s/mm^2 after three averages (ie, in line with the processing of the clinical data for the patient cohort, with eight averages used for b = 800). For each dataset (noise-free; SNR 10; SNR 20; SNR 40) and sample (10,000), RED values were calculated over the full domain of possible intermediate b values (b_{interm} = 1–799 s/mm^2; integer increments), with the first and last b values fixed at b = 0 and 800 s/mm^2, respectively. Simplified IVIM parameters, D_s and f_s, were also calculated similarly from the synthetic data for comparison.

Statistical Analysis

The within-subject coefficient of variation (WCV) was calculated to assess the ROI-based within-patient repeatability of RED in the volunteer cohort.

First, for each ROI of the volunteer cohort, the CV over time of the ROI mean RED value was calculated as given by Eq. 6, where X_{ROI} represents the vector of mean RED values at the 3 different imaging sessions:

$$CV_{ROI} = \frac{SD(X_{ROI})}{mean(X_{ROI})} \quad (6)$$

Subsequently, the WCV, ie, repeatability, was estimated by combining all of the individual ROI CVs according to Eq. 7, where N is the total number of ROIs:

$$WCV = \sqrt{\sum_{n=1}^{N} {CV_{ROI}^n}^2 / N} \quad (7)$$

Parameter repeatability was defined as excellent when WCV was ≤0.1, good between 0.1–0.2, acceptable between 0.2–0.3, and poor when MdAPD was >0.3, as defined in Kakite et al.[21] The 95% confidence intervals were similarly calculated using the above root mean square (RMS) method.[22] The significance of differences in WCV using different intermediate b values was tested by applying the Wilcoxon signed-rank test to the paired sets of squared individual ROI CVs.

The median absolute percentage deviation (MdAPD), a nonparametric analog to the CV, was calculated to assess the voxel-based precision in simulations and in the optimization cohort. The MdAPD was chosen in favor of the CV because it is much more robust to the presence of outliers in the voxelwise data. In Eq. 8, Y represents either the RED values of all 10,000 samples in the simulations, or the RED values of all voxels in all ROIs of all patients, for the given intermediate b value:

$$MdAPD = \frac{median(|Y - median(Y)|)}{median(Y_T)} \times 100 \quad (8)$$

To avoid points of divergence in the simulations where RED approaches 0 (eg, at high intermediate b values), MdAPD was set relative to median(Y_T) rather than median(Y), where Y_T represents the RED values obtained from the noise-free simulated data. Furthermore, to allow for direct comparison with the simulations, the same values were used in the denominator of Eq. 8 for calculating the MdAPD of the experimental data. Similarly, in calculating MdAPD for the simplified IVIM parameters D_s and f_s, the vector Y_T in Eq. 8 contained instead the corresponding specified full IVIM parameter values used in the simulations.

Receiver-operating characteristic (ROC) curve analysis was used to assess the performance of parameters in discriminating between healthy tissue and tumors (RED), as well as between true- and false-positive PI-RADS findings (RED, ADC, D_s, f_s), in the

diagnostic cohort. The significance of differences in imaging parameters between healthy tissue and tumors was tested with the Wilcoxon signed-rank test, while the difference between true- and false-positive PI-RADS findings was tested with the Mann-Whitney *U*-test. $P < 0.05$ was considered significant.

Logistic regression was performed to assess the diagnostic performance of different combinations of parameters (RED, ADC, *D*, *f*) for false-positive vs. true-positive findings. Permutation testing was performed to test for significance, by randomizing cancer status (true- and false-positive) for the samples, repeating the analysis 1000 times for each combination. The *P*-value was calculated as the proportion of permuted models achieving an equal or lower error than the nonpermuted models. The correlation between RED and ADC was assessed using the Pearson correlation coefficient, as well as the correlation between ADC values from the protocol used at our institution (b = 50, 800 s/mm^2) and ADC values from our suggested protocol (b = 0, 150, 800 s/mm^2), which also allows for the calculation of RED and simplified IVIM parameters. All analyses were performed in MatLab R2017a (MathWorks, Natick, MA).

Results

Protocol Optimization

Figure 1 shows RED as a function of an intermediate *b* value in the optimization cohort as boxplots, with overlapping calculations of RED from the Monte Carlo simulations assuming different SNRs. The IVIM parameter values (mean ± standard deviation) used for the simulations were D ($\times 10^{-3}$ mm^2/s) = 1.52 ± 0.27, D^* ($\times 10^{-3}$ mm^2/s) = 7.79 ± 2.85, and f = 0.12 ± 0.031 in the PZ, and D ($\times 10^{-3}$ mm^2/s) = 1.27 ± 0.13, D^* ($\times 10^{-3}$ mm^2/s) = 10.09 ± 3.25, and f = 0.14 ± 0.026 in the TZ. Both the experimental data and the simulations show that RED decreases with increasing intermediate *b* value, indicating the highest sensitivity to perfusion at lower intermediate *b* values. The simulations show that the median RED for noisy data with SNR ≥20 matches the median noise-free RED over a large range of intermediate *b* values, but the interquartile range increases substantially as the SNR decreases. The simulated RED values were in general found to agree with the experimental data (see Appendix 2 for corresponding plots of the simplified IVIM parameters). The best agreement is seen when assuming a SNR of 40 for the simulations (red line).

Figure 2 shows boxplots of precision as a function of an intermediate *b* value in the optimization cohort for both the PZ and TZ, with overlapping calculations of precision from the Monte Carlo simulations assuming different SNRs. The precision in the optimization cohort and the simulations appear to be in general agreement. The simulations imply that the best precision (lowest MdAPD) should be achieved using an intermediate *b* value in the range of 150–250 s/mm^2, regardless of SNR, as observed also in the experimental data (see also Appendix 3 for corresponding plots of accuracy and bias, and Appendix 4 for plots of precision, accuracy, and bias for the simplified IVIM parameters). The best agreement between the experimental data and the simulations is again seen when assuming an SNR of 40 in the simulations.

In the volunteer cohort, the repeatability over time was acceptable (0.2–0.3) for all intermediate *b* values tested, in both the PZ and TZ, apart from b = 50 s/mm^2 (0.3–0.4), as illustrated in Fig. 3. The median WCV values for the PZ were 0.38 (b = 50), 0.28 (b = 150), 0.28 (b = 250), 0.26 (b = 400). The median WCV values for the TZ were 0.39 (b = 50), 0.29 (b = 150), 0.25 (b = 250), 0.24 (b = 400). There was a significant difference in WCV between b = 50 and the other *b* values ($P < 0.05$), but not between these higher *b* values (b = 150, 250, and 400 s/mm^2). Using the same method, the median WCV values of ADC (Appendix 5) for both zones was shown to be between 0.096 and 0.098

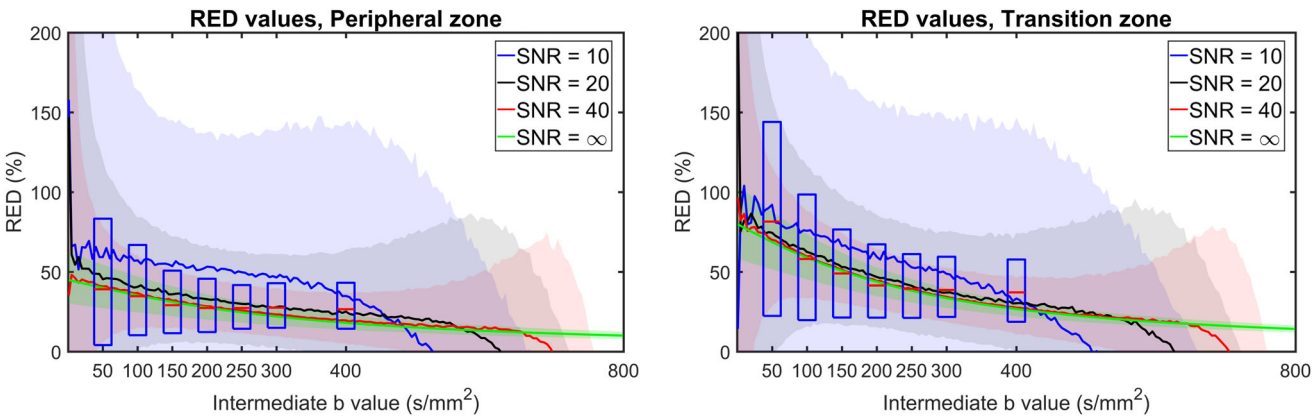

FIGURE 1: Boxplot showing RED as a function of intermediate *b* value in the optimization cohort, with overlapping Monte Carlo simulations showing RED as a function of intermediate *b* value, assuming different SNRs, for both the PZ (left) and the TZ (right). The solid continuous lines represent the median RED values from the simulations and the shaded areas the corresponding interquartile ranges. The boxplots represent the median RED values (horizontal red lines) and interquartile ranges (blue boxes) from the experimental data.

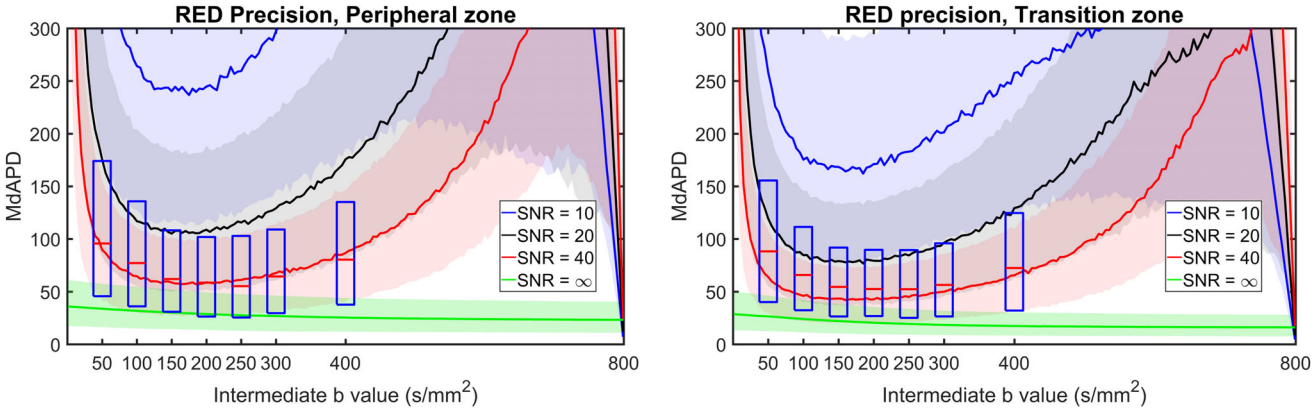

FIGURE 2: Boxplot showing precision of RED as a function of intermediate *b* value in the optimization cohort, with overlapping Monte Carlo simulations showing precision of RED as a function of intermediate *b* value, assuming different SNRs, for both the PZ (left) and the TZ (right). The solid continuous lines represent the median MdAPD values from the simulations and the shaded areas the corresponding interquartile ranges. The boxplots represent the median MdAPD values (horizontal red lines) and interquartile ranges (blue boxes) from the experimental data.

for the *b* values 0, 150, 250, and 400 s/mm^2, which was significantly lower than all the WCV values calculated for RED.

Figures 2 and 3 suggest that RED calculations using an intermediate *b* value in the range of 150–250 s/mm^2 would be optimal. Because of the higher SNR in lower *b* value images (Appendix 6), RED using an intermediate *b* value of b = 150 s/mm^2 was examined closer regarding diagnostic potential.

Diagnostic Potential of RED

Of the 32 suspicious lesions (PI-RADS ≥3), 14 were true-positive in the PZ, six true-positive in the TZ, 10 false-positive (ie, positive PI-RADS, negative biopsy) in the PZ, and two false-positive in the TZ. Because of the low sample size in the TZ (n = 6 true-positive, n = 2 false-positive), we only investigated the PZ and the combination of the PZ + TZ. Figure 4 shows the difference in mean RED (b = 0, 150, 800 s/mm^2) between biopsy-confirmed tumor tissue and contralateral healthy tissue, and ROC curves, for both the PZ and the combination of PZ + TZ. There was a significant difference in RED between tumor and contralateral healthy tissue for both the PZ (P < 0.001) and PZ + TZ (P < 0.001). The area under the curve (AUC) was 0.85 and 0.84 for the PZ and PZ + TZ, respectively. Similar results (AUC = 0.73 and 0.79) were obtained for RED using an intermediate *b* value of b = 250 s/mm^2 (see Appendix 7). For comparison, the AUC for ADC (0.99 and 0.99) was close to 1, but these values are likely biased due to the ROI placement on ADC maps.

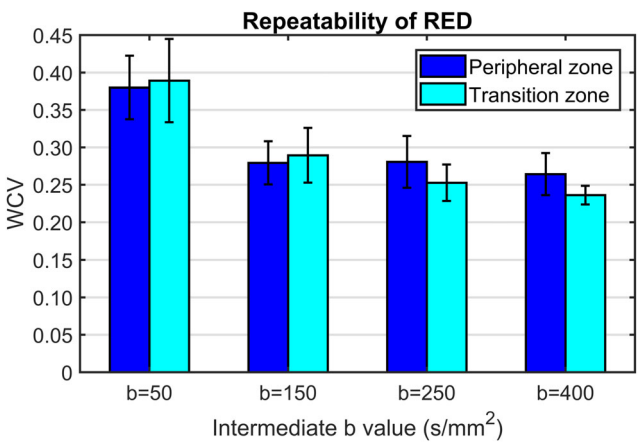

FIGURE 3: Grouped bar chart showing repeatability of RED (within-subject coefficient of variation, WCV) as a function of intermediate *b* value in the volunteer cohort, for the peripheral zone (blue) and transition zone (cyan). The error bars represent the 95% confidence intervals.

Table 2 shows the results of the logistic regression analysis of RED, ADC, and simplified IVIM parameters f_s and D_s in differentiating between false-positive PI-RADS findings and biopsy-confirmed tumors, with mean values and relative difference in mean value between false-positive healthy tissue and true-positive tumor tissue for the different parameters. The differences between false-positive tissue and tumors were not significant in the PZ for RED (P = 0.084), ADC (P = 0.057), or f (P = 0.46) but was significant for D (P = 0.024). Various combinations of parameters resulted in higher AUCs, which were generally significant in the PZ and in the PZ + TZ.

Figure 5 shows different parametric maps overlaid on a T_2-weighted map using the *b* values 0, 150, and 800 s/mm^2 for the calculation of RED, ADC, and the simplified IVIM parameters f_s and D_s, for one patient with a malignant lesion in the peripheral zone (PIRADS 5, PSA 22.4, Gleason score 4 + 5).

A moderate negative correlation was observed between RED and ADC using *b* values of 0, 150, and 800 s/mm^2 (rho = –0.453, P < 0.001), which indicates that the parameters probe distinct physiological processes (see Appendix 8). Furthermore, there was a near-perfect correlation of 0.998 (P <

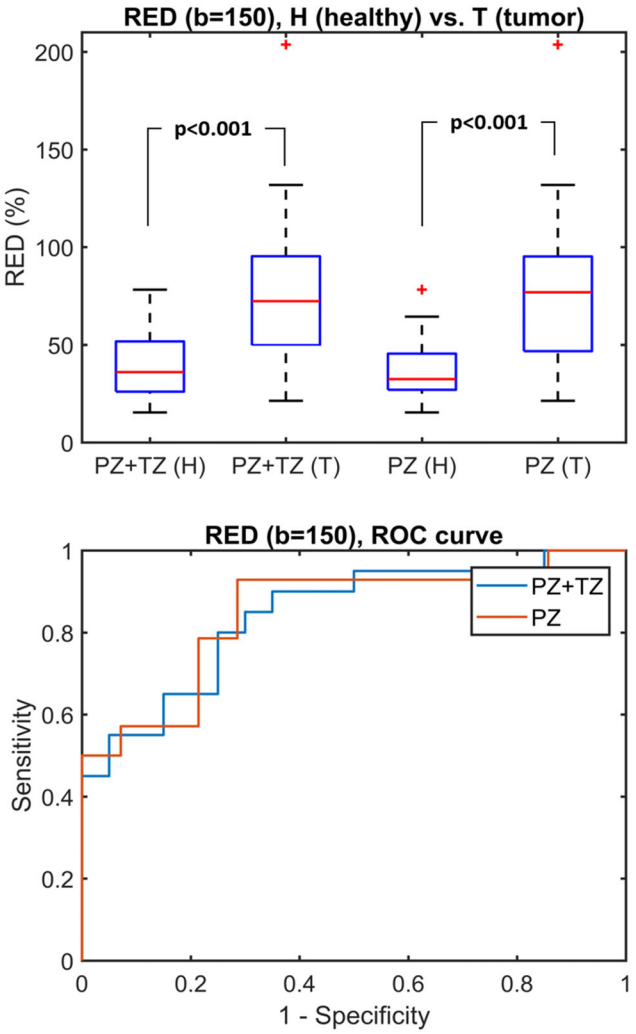

FIGURE 4: Box-and-whisker plot showing mean RED as a function of zone (PZ + TZ vs. PZ), and healthy (H) vs. tumor (T). ROC curve for RED using an intermediate *b* value of 150 s/mm^2, with AUC values of 0.84 and 0.85 for the PZ + TZ (lesion *n* = 20) and PZ (lesion *n* = 14), respectively.

0.001, slope = 0.98, intercept = 51) between the ADC values from the protocol used at our institution (b = 50, 800 s/mm^2) and ADC values from our suggested protocol (b = 0, 150, 800 s/mm^2), which also allows for the calculation of RED and simplified IVIM parameters (see Appendix 8).

Discussion

The number of PCa patients are increasing,[23–25] and so is the demand for prostate MR imaging. The commonly used mpMRI protocol takes between 30 and 45 minutes. Shorter MRI protocols are desirable to reduce pressure on the healthcare system. RED has previously been proposed as a fast and simple way to extract perfusion information from DW images acquired with three *b* values,[13] without the use of contrast. In this study, we showed that the optimal intermediate *b* value for RED imaging in the prostate is between 150 and 250 mm/s^2, and that RED was reproducible over time. RED was also shown to differentiate cancer from healthy tissue and could aid in finding biopsy-positive lesions.

PI-RADS v. 2 recommends that DWI include a low *b* value at 50–100 s/mm^2 and a high *b* value at 800–1000 s/mm^2, with optional intermediate *b* values between 100–1000 s/mm^2 for more accurate ADC calculations.[3] Consequently, only minor adjustments to the DWI protocol are required for the calculation of RED (and simplified IVIM parameters D_s and f_s), which would have limited impact on the total scan time (an increase of <30 sec in most cases). Furthermore, we showed that ADC calculated with *b* values of 50 and 800 s/mm^2 and with 0, 150, and 800 s/mm^2 had a near-perfect correlation.

The healthy RED values were similar for the patients in the optimization and diagnostic cohort, but were in general higher for the asymptomatic healthy volunteers, which can partially be explained by the age-related differences in the prostate. We showed that RED was dependent on the intermediate *b* value, especially in the PZ. The precision plots suggested that an optimal intermediate *b* value for minimizing the sensitivity to noise is in the range of 150–300 s/mm^2 for both the PZ and TZ. This finding was confirmed by the repeatability analysis, showing a significantly worse repeatability using b = 50 s/mm^2 in comparison with the rest. Further support for this optimal range was provided by simulations of accuracy and bias. An intermediate *b* value in the lower range, eg, b = 150 s/mm^2, makes RED more sensitive to perfusion and allows for images with a higher SNR, because of the higher signal at lower *b* values. However, an even lower intermediate *b* value risks reduced precision and repeatability and mixing of perfusion effects into the high *b* value regime (ADC_{high}). An intermediate *b* value in the higher range, eg, b = 250 s/mm^2, gives more reliable estimates of f_s and D_s because of the better separation of perfusion and perfusion-free areas, but at the cost of lower SNR. Using the calculated full IVIM parameters, it was estimated that perfusion effects contributed to less than 5% of the signal in the high *b* value regime when the intermediate *b* value was set to 150 mm/s^2. The measured SNR for our experimental data using a subset of patients (*n* = 5), calculated using the difference method as described by Dietrich et al[26] was found to be (median (range)) 20 (13.1–31.1) for the b = 0 s/mm^2 images in both the PZ and TZ. The experimental RED precision was found to be within the 25th and 75th percentile of the simulated precision, with an SNR of 20, although the median values were closer to those of simulations with an SNR of 40.

While et al[19] investigated the optimal intermediate *b* value for breast and liver tissue using the same simulation method as described in this article, and found that 100 s/mm^2 for breast and 50 s/mm^2 for liver imaging (given low and high *b* values of 0 and 700 s/mm^2) was optimal for limiting the impact of noise. Liver tissue is in general more

TABLE 2. Logistic Regression Analysis of the Ability of Different Combinations of RED, ADC, f_s, and D_s in Discriminating Between False-Positive Lesions and Biopsy-Confirmed Tumors

False positive lesions vs. cancer			
PZ + TZ, parameter mean (standard deviation)			
Parameter	False positive (FP)	Tumor (T)	Relative difference (%)
RED (%)	53.75 (48.87)	77.72 (40.18)	36.5
ADC (x10^{-3} mm^2/s)	1.09 (0.17)	0.92 (238.63)	–16.9
f_s	0.059 (0.050)	0.079 (0.031)	29.0
D_s (x10^{-3} mm^2/s)	1.03 (0.17)	0.85 (0.23)	–19.1
PZ, parameter mean (standard deviation)			
	False positive (FP)	Tumor (T)	Relative difference (%)
RED (%)	51.62 (53.72)	80.67 (46.16)	43.9
ADC (x10^{-3} mm^2/s)	1.13 (0.15)	0.91 (261.10)	–21.6
f_s	0.059 (0.055)	0.079 (0.037)	29.0
D_s (x10^{-3} mm^2/s)	1.08 (0.15)	0.84 (0.25)	–25.0
AUC values			
Parameter (unit)	PZ + TZ	PZ	
RED	0.70*	0.71	
ADC	0.71*	0.74	
f_s	0.61	0.59	
D_s	0.74*	0.78*	
RED + ADC	0.73	0.77	
RED + D_s	0.76*	0.81*	
f_s + D_s	0.78*	0.83*	
ADC + f_s + D_s	0.79*	0.84*	
RED + ADC + f_s + D_s	0.88*	0.91*	

Mean values and relative difference in mean value between healthy and tumor for the different parameters. The sample size for the PZ was n = 10 false-positive lesions and 14 biopsy-confirmed tumors. The sample sizes were 2 and 6 for the TZ, respectively.
RED (relative enhanced diffusivity), ADC (apparent diffusion coefficient), f (perfusion fraction), D (diffusion coefficient), FP (false positive), T (tumor), Relative difference = 100*(T-FP)/avg(T,FP).
*$P < 0.05$.

perfused than the prostate,[27–29] which leads to faster signal decay at lower b values, and therefore a lower optimal intermediate b value for minimizing the impact of noise.

The logistic regression analysis showed how RED could aid in differentiating between false-positive PI-RADS findings and biopsy-confirmed lesions in the PZ. The low sample size in the TZ made the analysis sensitive to overfitting and therefore no conclusions can be made regarding the performance of the different parameters in the TZ. In the logistic regression analysis, RED performed better than the perfusion fraction f_s in discriminating between false-positive and true-positive tissue, but the diffusion coefficient D_s was the best-performing single parameter. This agrees with the literature investigating the full IVIM approach in PCa, where D outperforms f and the pseudodiffusion coefficient D*.[7,30] ADC + RED performed better than ADC alone, while combining all the parameters performed better than ADC + f + D, with an AUC of 0.907 for the PZ. These results show that RED in combination with the other parameters may be able to help prevent false-positive PI-RADS findings.

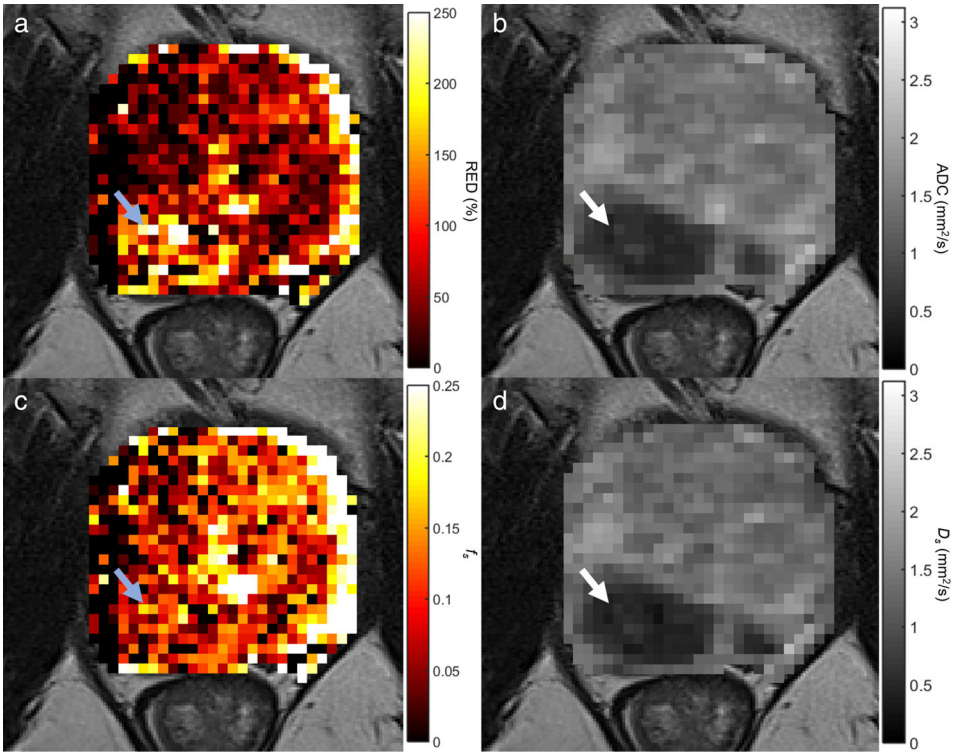

FIGURE 5: Representative parametric maps using the *b* values 0, 150, and 800 s/mm^2, obtained for a 72-year-old man with biopsy-proven prostate cancer in the peripheral zone (PIRADS 5, PSA 22.4, Gleason score 4 + 5). Parametric maps of (a) RED, (b) ADC and simplified IVIM parameters (c) f_s and (d) D_s, overlaid on a T_2-weighted image. The arrows in each image point at the same biopsy-confirmed cancer lesion.

There were 12 false-positive lesions in the diagnostic cohort, 10 in the PZ, and two in the TZ, defined as positive PI-RADS, but negative biopsies. Most of the patients in the diagnostic cohort underwent systematic biopsies (n = 16), with one patient having targeted MRI-TRUS fusion biopsy. In the case of systematic biopsies, the decision to classify a lesion as true-positive was made when the PI-RADS lesion and positive biopsy were in the same anatomical area in the prostate, as described in PI-RADS 2.0.[3] This can lead to some uncertainty when assessing if the cancer and radiological findings are the same, which is less of a problem for targeted biopsies.

As demonstrated by While et al,[19] RED can be viewed as a simple reparameterization of IVIM modeling in the limit of only three b values (ie, explicitly omitting D*), as proposed in the original IVIM article.[5] Nonetheless, this study indicates that RED might have potential to provide additional discriminatory power if used in addition to other parameters, such as ADC, f_s, and D_s. Similar results were found by Vidic et al, who investigated the combination of ADC, RED, and IVIM in breast cancer.[31]

An obvious weakness of the RED parameter is the high sensitivity to noise compared with the ADC parameter, which would limit its application as a single biomarker for PCa in clinical practice. Although relative differences between false-positive and true-positive findings were larger for RED than for ADC, RED was also associated with higher standard deviations and significantly lower repeatability. While et al[19] found that RED in general displays greater sensitivity to noise than the perfusion fraction f_s alone, because RED compounds errors associated with both f_s and D_s. However, this study showed that when averaging over ROIs with clinically realistic sizes, repeatability was acceptable and an additional value of RED in combination with other DWI parameters was demonstrated.

The full IVIM parameters (f, D, and D* from Eq. 3) used for generating the simulated data in the optimization cohort were calculated from a suboptimal set of b values, potentially not sufficiently sampling the signal in the b = 0–100 s/mm^2 range, as recommended when performing IVIM.[28] Nevertheless, the IVIM parameter values in this study were in the same range as previously reported for the prostate.[7,29,32–34] The simplified IVIM parameters from Eqs. 4 and 5 were, on the other hand, entirely valid, since they only depend on three b values. Finally, the simulations were restricted to a simple Rician noise model, and did not include physiological noise or other artifacts. Nevertheless, the correspondence between the simulations and experiments suggests that these latter effects were minimal.

Limitations

The results of this work are limited by the small cohorts, especially in the diagnostic cohort. Stratification of patients

into different Gleason grade groups was therefore not possible and the results need to be validated in a larger and more heterogeneous cohort. There were only a limited number of TZ tumors in the diagnostic cohort, which made significance testing and logistic regression analysis unreliable for lesions in this zone. Another issue when calculating RED in the TZ is that the difference in perfusion between healthy tissue and cancer in the TZ is small compared to the PZ,[35] which can be explained by the presence of highly perfused benign prostate hyperplasia (BPH). Another limitation is that most patients underwent systematic instead of targeted biopsies. Because of the preliminary nature of this study, only a limited cohort size was available for the logistic regression analysis comparing false-positive and true-positive lesions. Ideally, cross-validation should be performed to test the predictive performance against overfitting, which was not possible in this dataset, and should be investigated in a larger dataset with independent training and test sets.

In conclusion, RED appears to be a repeatable biomarker that may have value for PCa diagnosis. The optimal intermediate b value for minimizing noise and maximizing repeatability is between 150 and 250 s/mm^2. These results provide a solid basis for further investigation of the value of RED in larger and more heterogeneous PCa cohorts, including comparison with perfusion measurements from DCE-MRI and IVIM models.

Acknowledgments

We thank Kjerstin Olaussen, Research Nurse at St. Olavs Hospital, Trondheim University Hospital, and Torill E. Sjøbakk, Senior Engineer at NTNU, Norwegian University of Science and Technology, for help in administrating patient recruitment, consent forms, and data collection. MR services were jointly provided by St. Olavs Hospital, Trondheim University Hospital, and the MR Core Facility at NTNU, Norwegian University of Science and Technology.

References

1. Barentsz JO, Richenberg J, Clements R, et al. ESUR prostate MR guidelines 2012. Eur Radiol 2012;22:746–757.
2. Koh DM, Collins DJ. Diffusion-weighted MRI in the body: Applications and challenges in oncology. AJR Am J Roentgenol 2007;188:1622–1635.
3. Weinreb JC, Barentsz JO, Choyke PL, et al. PI-RADS Prostate Imaging — Reporting and Data System: 2015, Version 2. Eur Urol 2016;69:16–40.
4. Le Bihan D, Turner R. The capillary network: A link between IVIM and classical perfusion. Magn Reson Med 1992;27:171–178.
5. Le Bihan D, Breton E, Lallemand D, Aubin ML, Vignaud J, Laval-Jeantet M. Separation of diffusion and perfusion in intravoxel incoherent motion MR imaging. Radiology 1988;168:497–505.
6. Koh DM, Collins DJ, Orton MR. Intravoxel incoherent motion in body diffusion-weighted MRI: Reality and challenges. AJR Am J Roentgenol 2011;196:1351–1361.
7. Valerio M, Zini C, Fierro D, et al. 3T multiparametric MRI of the prostate: Does intravoxel incoherent motion diffusion imaging have a role in the detection and stratification of prostate cancer in the peripheral zone? Eur J Radiol 2016;85:790–794.
8. Yang DM, Kim HC, Kim SW, et al. Prostate cancer: Correlation of intravoxel incoherent motion MR parameters with Gleason score. Clin Imaging 2016;40:445–450.
9. Chandarana H, Kang SK, Wong S, et al. Diffusion-weighted intravoxel incoherent motion imaging of renal tumors with histopathologic correlation. Invest Radiol 2012;47:688–696.
10. Fujima N, Yoshida D, Sakashita T, et al. Intravoxel incoherent motion diffusion-weighted imaging in head and neck squamous cell carcinoma: Assessment of perfusion-related parameters compared to dynamic contrast-enhanced MRI. Magn Reson Imaging 2014;32:1206–1213.
11. Liu C, Wang K, Chan Q, et al. Intravoxel incoherent motion MR imaging for breast lesions: Comparison and correlation with pharmacokinetic evaluation from dynamic contrast-enhanced MR imaging. Eur Radiol 2016;26:3888–3898.
12. Le Bihan D. What can we see with IVIM MRI? Neuroimage 2019;187:56–67.
13. Teruel JR, Goa PE, Sjobakk TE, Ostlie A, Fjosne HE, Bathen TF. A simplified approach to measure the effect of the microvasculature in diffusion-weighted MR imaging applied to breast tumors: Preliminary results. Radiology 2016;281:373–381.
14. Niu XK, Chen XH, Chen ZF, Chen L, Li J, Peng T. Diagnostic Performance of biparametric MRI for detection of prostate cancer: A systematic review and meta-analysis. AJR Am J Roentgenol 2018:1–10.
15. Kuhl CK, Bruhn R, Kramer N, Nebelung S, Heidenreich A, Schrading S. Abbreviated biparametric prostate MR imaging in men with elevated prostate-specific antigen. Radiology 2017;285:493–505.
16. Junker D, Steinkohl F, Fritz V, et al. Comparison of multiparametric and biparametric MRI of the prostate: Are gadolinium-based contrast agents needed for routine examinations? World J Urol 2019;37:691–699.
17. De Visschere P, Lumen N, Ost P, Decaestecker K, Pattyn E, Villeirs G. Dynamic contrast-enhanced imaging has limited added value over T2-weighted imaging and diffusion-weighted imaging when using PI-RADSv2 for diagnosis of clinically significant prostate cancer in patients with elevated PSA. Clin Radiol 2017;72:23–32.
18. Ramalho J, Semelka RC, Ramalho M, Nunes RH, AlObaidy M, Castillo M. Gadolinium-based contrast agent accumulation and toxicity: An update. AJNR Am J Neuroradiol 2016;37:1192–1198.
19. While PT, Teruel JR, Vidic I, Bathen TF, Goa PE. Relative enhanced diffusivity: Noise sensitivity, protocol optimization, and the relation to intravoxel incoherent motion. MAGMA 2018;31:425–438.
20. Wurnig MC, Donati OF, Ulbrich E, et al. Systematic analysis of the intravoxel incoherent motion threshold separating perfusion and diffusion effects: Proposal of a standardized algorithm. Magn Reson Med 2015;74:1414–1422.
21. Kakite S, Dyvorne H, Besa C, et al. Hepatocellular carcinoma: Short-term reproducibility of apparent diffusion coefficient and intravoxel incoherent motion parameters at 3.0T. J Magn Reson Imaging 2015;41:149–156.
22. Bland M. *How should I calculate a within-subject coefficient of variation?* Vol. 2019. York, UK: University of York; 2006.
23. Ferlay J, Shin HR, Bray F, Forman D, Mathers C, Parkin DM. Estimates of worldwide burden of cancer in 2008: GLOBOCAN 2008. Int J Cancer 2010;127:2893–2917.
24. Ferlay J, Soerjomataram I, Dikshit R, et al. Cancer incidence and mortality worldwide: Sources, methods and major patterns in GLOBOCAN 2012. Int J Cancer 2015;136:E359–386.
25. Bray F, Ferlay J, Soerjomataram I, Siegel RL, Torre LA, Jemal A. Global cancer statistics 2018: GLOBOCAN estimates of incidence and mortality worldwide for 36 cancers in 185 countries. CA Cancer J Clin 2018;68:394–424.

26. Dietrich O, Raya JG, Reeder SB, Reiser MF, Schoenberg SO. Measurement of signal-to-noise ratios in MR images: Influence of multichannel coils, parallel imaging, and reconstruction filters. J Magn Reson Imaging 2007;26:375–385.

27. Valentin J. Basic anatomical and physiological data for use in radiological protection: Reference values: ICRP Publication 89: Approved by the Commission in September 2001. Ann ICRP 2002;32:1–277.

28. Lemke A, Stieltjes B, Schad LR, Laun FB. Toward an optimal distribution of b values for intravoxel incoherent motion imaging. Magn Reson Imaging 2011;29:766–776.

29. Dopfert J, Lemke A, Weidner A, Schad LR. Investigation of prostate cancer using diffusion-weighted intravoxel incoherent motion imaging. Magn Reson Imaging 2011;29:1053–1058.

30. Pesapane F, Patella F, Fumarola EM, et al. Intravoxel incoherent motion (IVIM) diffusion weighted imaging (DWI) in the periferic prostate cancer detection and stratification. Med Oncol 2017;34:35.

31. Vidic I, Egnell L, Jerome NP, et al. Support vector machine for breast cancer classification using diffusion-weighted MRI histogram features: Preliminary study. J Magn Reson Imaging 2018;47:1205–1216.

32. Shi C, Zhang D, Xiao Z, et al. Ultrahigh b-values MRI in normal human prostate: Initial research on reproducibility and age-related differences. J Magn Reson Imaging 2017;46:801–812.

33. Ueda Y, Takahashi S, Ohno N, et al. Triexponential function analysis of diffusion-weighted MRI for diagnosing prostate cancer. J Magn Reson Imaging 2016;43:138–148.

34. Kuru TH, Roethke MC, Stieltjes B, et al. Intravoxel incoherent motion (IVIM) diffusion imaging in prostate cancer — What does it add? J Comput Assist Tomogr 2014;38:558–564.

35. van Niekerk CG, Witjes JA, Barentsz JO, van der Laak JA, Hulsbergen-van de Kaa CA. Microvascularity in transition zone prostate tumors resembles normal prostatic tissue. Prostate 2013;73:467–475.